Int. J. Electrochem. Sci., 9 **(2014)** 778 - 798

International Journal of
ELECTROCHEMICAL
SCIENCE
www.electrochemsci.org

Effect of Hydrostatic Pressure on the Pitting Corrosion Behavior of 316L Stainless Steel

Zhongyi Wang[1], *Yuan Cong*[2], *Tao Zhang*[2,3,*]

[1]College of Power and Energy Engineering, Harbin Engineering University, Nantong ST 145, Harbin, 150001, China
[2] Corrosion and protection Laboratory, Key Laboratory of Superlight Materials and Surface Technology (Harbin Engineering University), Ministry of Education, Nantong ST 145, Harbin, 150001, China
[3] State Key Laboratory for Corrosion and Protection, Institute of Metal Research, Chinese Academy of Sciences, Wencui RD 62, Shenyang, 110016, China)
[*]E-mail: zhangtao@hrbeu.edu.cn

Received: 23 September 2013 / *Accepted:* 12 November 2013 / *Published:* 8 December 2013

The pitting corrosion behavior of 316L stainless steel (316L SS) was investigated by electrochemical measurements, nanoindentation and microscopy observation. The experiment results have been analyzed based upon the stochastic theory. Pitting initiation process has been modeled as anonhomogeneous Poisson process and analyzed using a Weibull distribution function. Pitting growth process has been simulated by a nonhomogeneous Markov process and analyzed using Gumbel distribution function. The analysis results revealed that hydrostatic pressure had three effects on the pitting corrosion behavior of 316L SS: (1) the increasing hydrostatic pressure enhance the mechanical properties of passive film; (2) the increasing hydrostatic pressure retarded the B1 process and accelerated the A3 process; (3) the pitting growth probability decreased with the increase of hydrostatic pressure. The above three factors led to the improvement of pitting corrosion resistance of 316L SS with the increasing of hydrostatic pressure.

Keywords: hydrostatic pressure; pitting corrosion; stochastic analysis; 316L SS; Deep Ocean

1. INTRODUCTION

Oil and gas exploitation in deep ocean environment imply challenging harsh corrosive environments for structural materials because of the hydrostatic pressure and the different dissolved oxygen (DO). Thus, the corrosion problem of materials in deep ocean condition must be considered.

Some natural ocean tests were reported by American [1-3], Indian [4, 5] and Russian [6, 7]. They revealed that materials undergo serious corrosion in deep ocean. However, deep ocean environment is a complex system: hydrostatic pressure, different DO, delicately balanced solution of many salts, suspended silt, and decaying organic material. The individual effect of each of the above factors affecting corrosion behavior is not readily distinguishable.

Some laboratory experiments simulating deep sea environment [9-14] were investigated, the results of which demonstrated that hydrostatic pressure was an ineligible aspect to material corrosion. Beccaria et al. [10] reported the effect of hydrostatic pressure on the corrosion of nickel, showing that by increasing the hydrostatic pressure, the corrosion rate and the susceptibility to pitting of nickel increased in NaCl solution and decreased in sea water because of the different nature of the corrosion layers formed in these solutions. And also influence of hydrostatic pressure on corrosion of aluminum and 6061-T6 aluminum alloy in sea water were studied by Beccaria and Poggi et al. [11, 15]. The results revealed that on increasing the hydrostatic pressure the corrosion of aluminum increased, mainly as a result of increasing in localized corrosion, and the average corrosion rate of 6061-T6 aluminum alloy decreased due to the formation of an Mg-Al oxide layer which was more protective than aluminum hydroxides. Our previous work also indicated that the hydrostatic pressure increased the corrosion susceptibility of Fe-20Cr alloy, Ni-Cr-Mo-V steel, Nickel and Zn anode [16-21]. However, there are a number of areas where the effects of hydrostatic pressure are not known, including its effect on the pitting corrosion resistance, such as pitting potential and passive current density, on the mechanical property of passive film, on the pitting initiation process, on the pitting geometry and on the pitting growth probability.

Pitting corrosion is a complicated phenomenon. The pitting generation event has been widely known to be a stochastic nature [22]. Recently, stochastic analysis has been proposed to investigate the pitting initiation processes. Localized corrosion of different metals or alloys in vary systems has been characterized in terms of stochastic analysis [23-34].

In the present work, the corrosion behavior of 316L SS was investigated through a series of laboratory test in 3.5% NaCl solution during which only the hydrostatic pressure was changed, all other parameters (DO, temperature, etc.) remaining constant. The effect of hydrostatic pressure on the corrosion of 316L SS was discussed.

2. EXPERIMENTAL

2.1. Materials

The material was 316L stainless steel (316L SS) whose main compositions were: 19.4% Cr, 11.8% Ni, 2.2% Mn, 2.4% Mo, 0.2% Si. All of the specimens were wet ground to a 1000-grit finish, degreased with acetone, cleansed with distilled water and dried in a compressed hot air flow. The test solution was 3.5% NaCl with a DO concentration of about 6.5 ppm.

2.2. Experimental setup

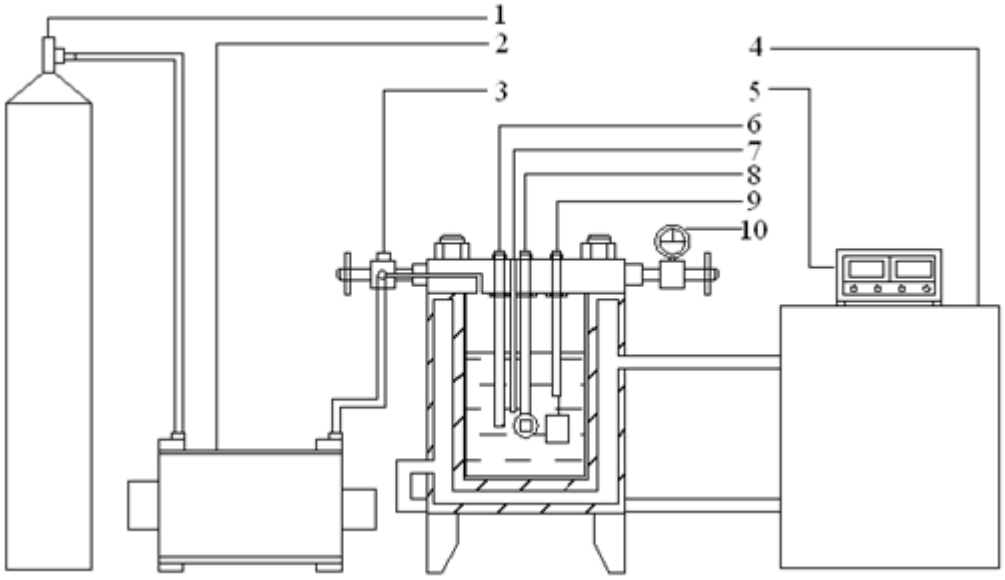

Figure 1. Schematic diagram of the experimental setup for deep ocean corrosion study. (1) nitrogen vessel, (2) hydropneumatic pump, (3) valve, (4) colling equipment, (5) temperature monitor, (6) solid-reference-electrode, (7) thermocouple, (8) working electrode, (9) counter electrode and (10) pressure meter.

The pressure vessel was shown in Fig.1, which was pressurized with a hydropneumatic pump by using high purity nitrogen. According to Henry' law, it can be believed that the oxygen pressure was unchanged with the increasing of nitrogen pressure. Nitrogen pressure has no influence on the DO concentration.

2.3. Electrochemical measurements

For all the experiments, a three-electrode cell was used with a counter electrode of platinum (20mm×20mm) and an Ag/AgCl reference electrode. The potential of the Ag/AgCl reference electrode was compared (within the pressure range 1-100 atm) with that of identical electrode maintained at 1 atm. The slight change (-5mV at 100 atm) of the pressurized Ag/AgCl reference electrode potential was noted in further measurements of the working electrode potential at various pressures. The test pressures were 1 atm and 80 atm.

The potentiodynamic polarization technique was used to determine the pitting potential of 316L SS. The potentiodynamic polarization curves with the scan rate 0.333mV/s were measured, which were carried out using a model 273A potentiostat (EG&G). At least thirty replicates were used for each potential sweep velocity. Prior to all electrochemical measurements, the specimens were initially reduced potentiostatically at $-1V_{SHE}$ for 1 min to remove air-formed oxides from the surface and then kept for 1hour in the NaCl solution at various hydrostatic pressures.

Induction time of 316L SS at various hydrostatic pressures was determined by chronoamperometry curve under a constant potential of 300 mV_{SHE}. Thirty replicates were used for the specimens.

2.3. Microstructure observation

2.3.1. SEM

The pitting morphology of 316L SS after the potentiostatic measurements were studied by means of an X-Max SEM.

2.3.2. Pitting mouth size and pitting depth measurement

The tested pitting was gently rinsed and dried for examination with an optical microscope. The size of the pitting mouth *s* was determined from photography by measuring the area of the pitting mouth with a planimeter in the microscope. The estimated error in *s* is 5%. Pitting depths *h*, which were treated with ultrasound to rupture the pitting lacy, were measured by applying the Fine Focus Technique [35], where the distances required shifting the optical objective between the focal points on the original surface of sample and on the bottom of the pitting is compared. The estimated error in *h* is 1μm.

3. RESULTS AND DISCUSSION

3.1. Effect of hydrostatic pressure on the pitting corrosion resistance of 316L SS

3.1.1. Potentiodynamic polarization

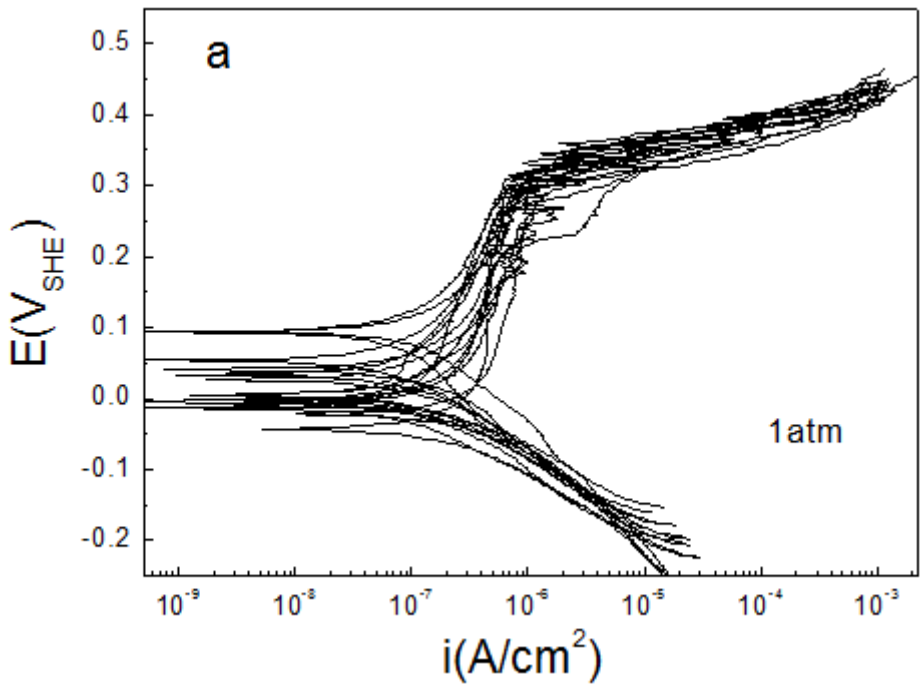

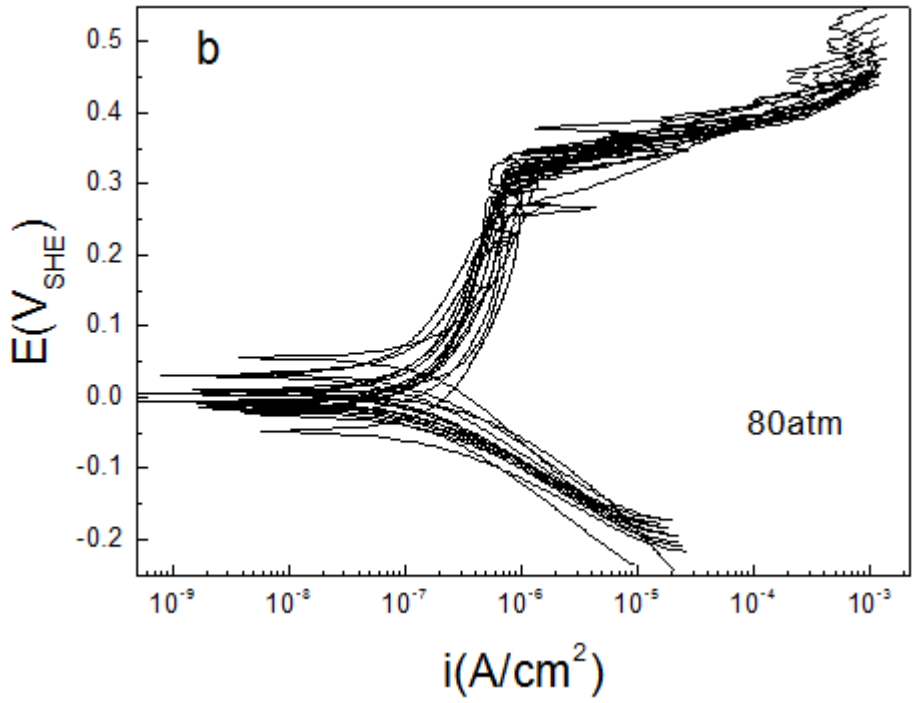

Figure 2. Potentiodynamic polarization curves of 316L SS at (a)1 atm and (b) 80 atm hydrostatic pressures.

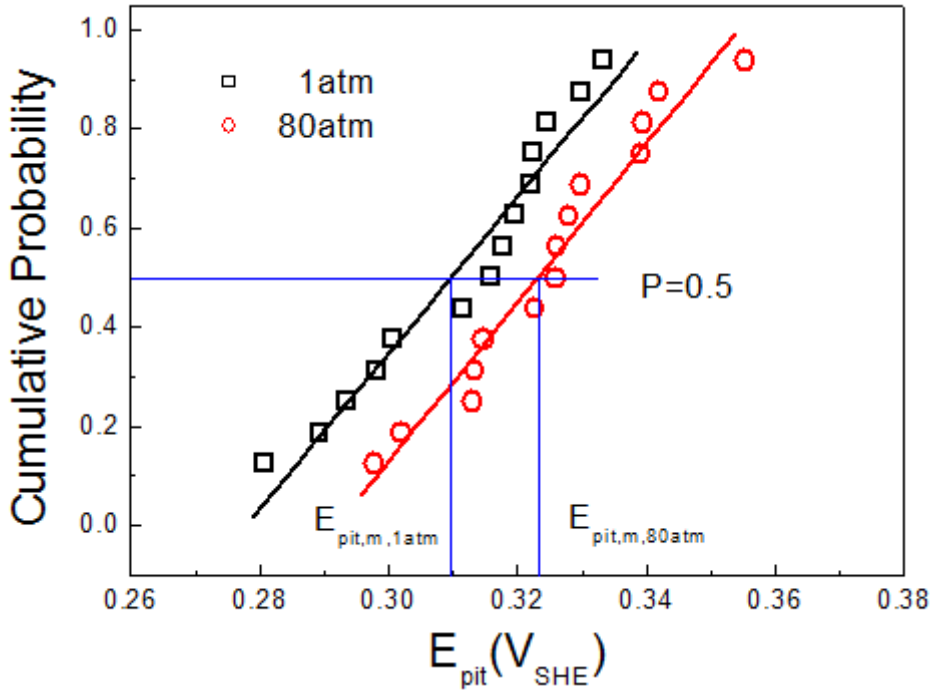

Figure 3. The distribution of pitting potential of 316L SS at (a) 1atm and (b) 80 atm hydrostatic pressure.

The polarization curves of 316L SS at various hydrostatic pressures were exhibited in Fig. 2. On the presented curves for each electrode, a pitting potential could be determined. It could be found

that the pitting potential data were scatted. The distributions of pitting potential for 316L SS at various hydrostatic pressures were plotted as illustrated in Fig. 3. Cumulative probability shown in a vertical abscissa was calculated by a mean rank method:

$$P_{cum} = i/(N+1) \qquad (1)$$

Where P_{cum} is the cumulative probability of measured pitting potential (E_{pit}), i is the order in the total number N (i = 1, 2, 3, …, N). All of the pitting potential distributions exhibited a linear behavior, indicating that the distribution of pitting potentials measured followed the normal probability distribution.

The median of distribution E_m, decided at P = 50%, was determined from Fig. 3. As can be seen from Fig. 3, the pitting potential E_m, shifts to the noble direction with hydrostatic pressure (increased from 309mV to 323 mV), suggesting that the pitting corrosion resistance was improved with the increasing of hydrostatic pressure.

3.1.2. Electrochemical impedance spectroscopy

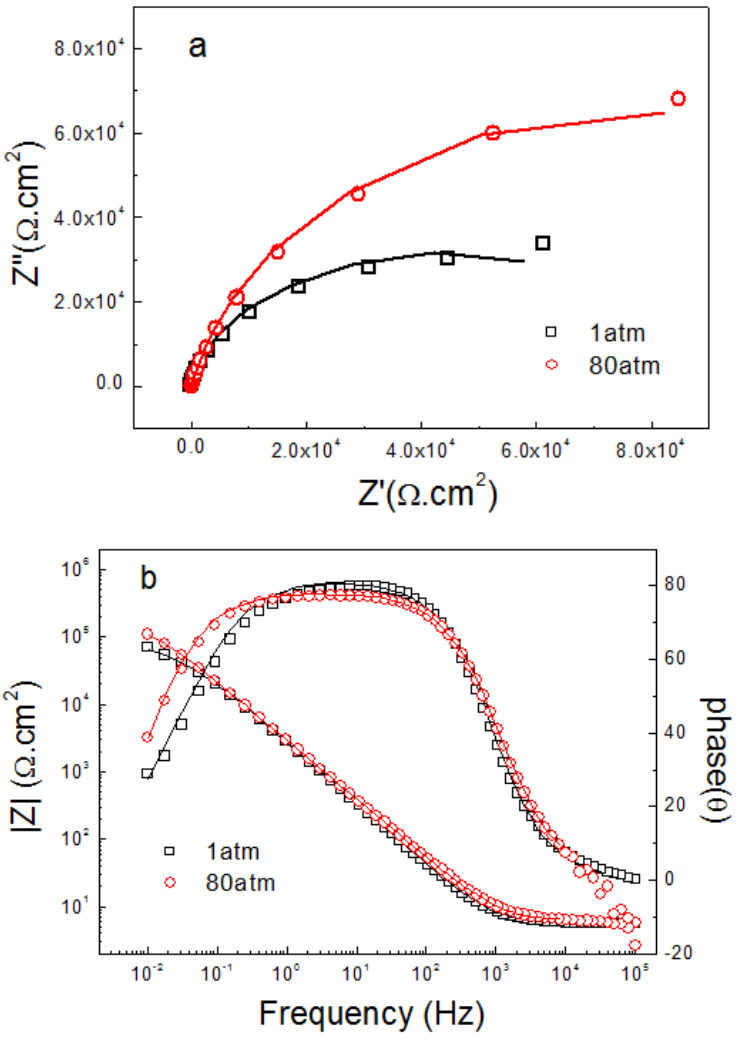

Figure 4. (a) Nyquist plot and (b) Bode plot of 316L SS at different hydrostatic pressures

The EIS results measured at different hydrostatic pressures were illustrated in Fig.4. The equivalent circuit in Fig. 5 was used to fit the EIS data.

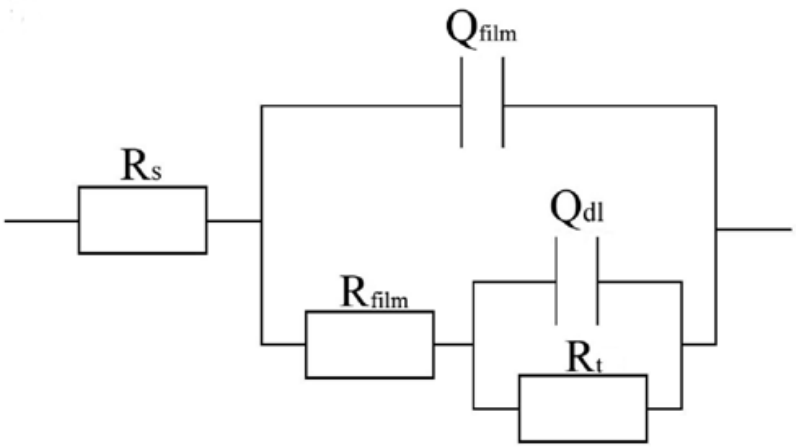

Figure 5. Equivalent circuits for EIS data

Where R_s was the solution resistance, Q_f was the capacitance of passive film and R_f was the resistance of passive film, Q_{dl} was the double layer capacitance, R_t was the charge transfer resistance. It could be observed that the equivalent circuits fit the experimental data well in most of the frequency range, and the fitted results were listed in Table 1.

Table 1. Element values of equivalent circuit to fit the impedance data in Fig.4

Hydrostatic pressure	$R_f(\Omega.cm^2)$	CPE_f		$R_t(\Omega.cm^2)$	CPE_{dl}	
		$Y_0(\Omega^{-1}.cm^{-2}.s^n)$	n		$Y_0(\Omega^{-1}.cm^{-2}.s^n)$	n
1 atm	1478	7.96×10^{-4}	0.79	—	—	—
60 atm	408	4.87×10^{-3}	0.74	677	9.13×10^{-4}	0.79

Both R_f and R_t of 316L SS increased with hydrostatic pressure, indicating the enhance of corrosion resistance, which was consistent with the results of potentiodynamic polarization.

3.2. Effect of hydrostatic pressure on the mechanic properties of passive film

Fig. 6 exhibited the typical load-depth curves measured with ex-situ indentation tests for 316L SS surfaces passivated at 300 mV_{SHE} at various hydrostatic pressures. In the unloading direction, the indentation depth decreased with decreasing load mainly due to the recovery of elastic deformation.

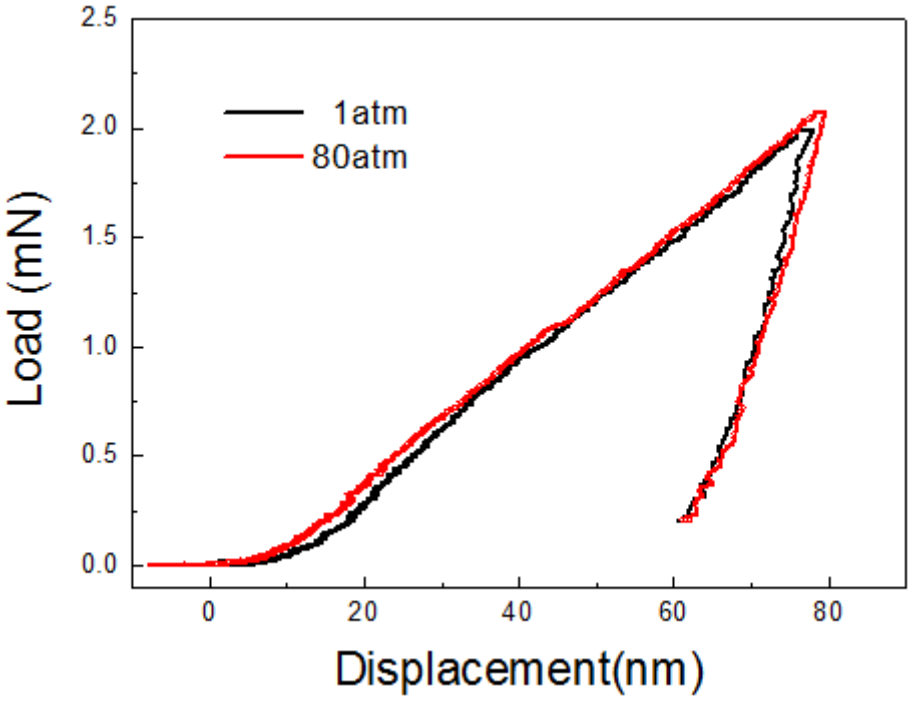

Figure 6. Load-depth curves for 316L SS surfaces passivated at 300 mV_{SHE} at various hydrostatic pressures.

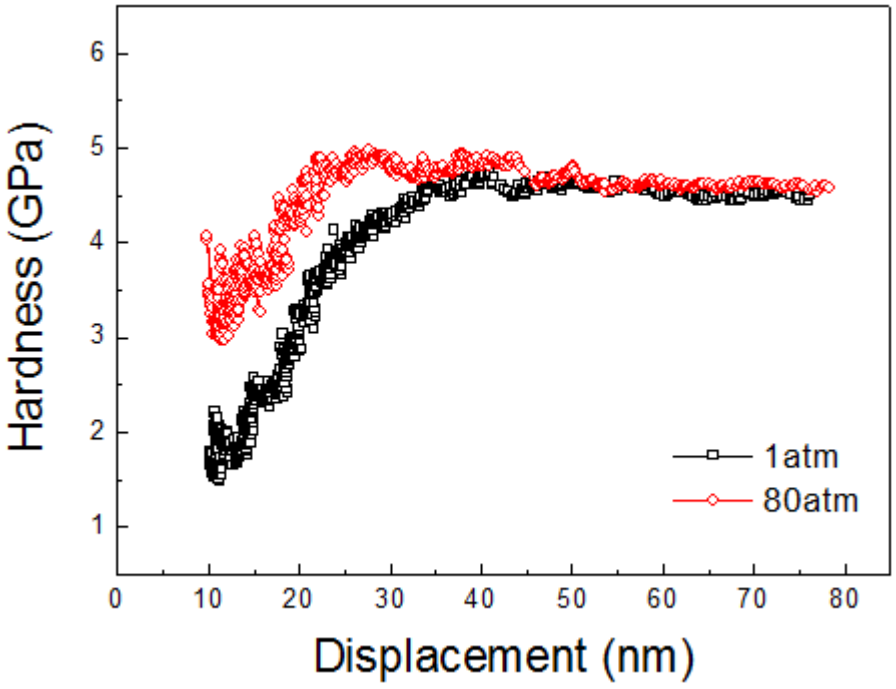

Figure 7. Hardness of passive film of 316L SS formed at various hydrostatic pressures

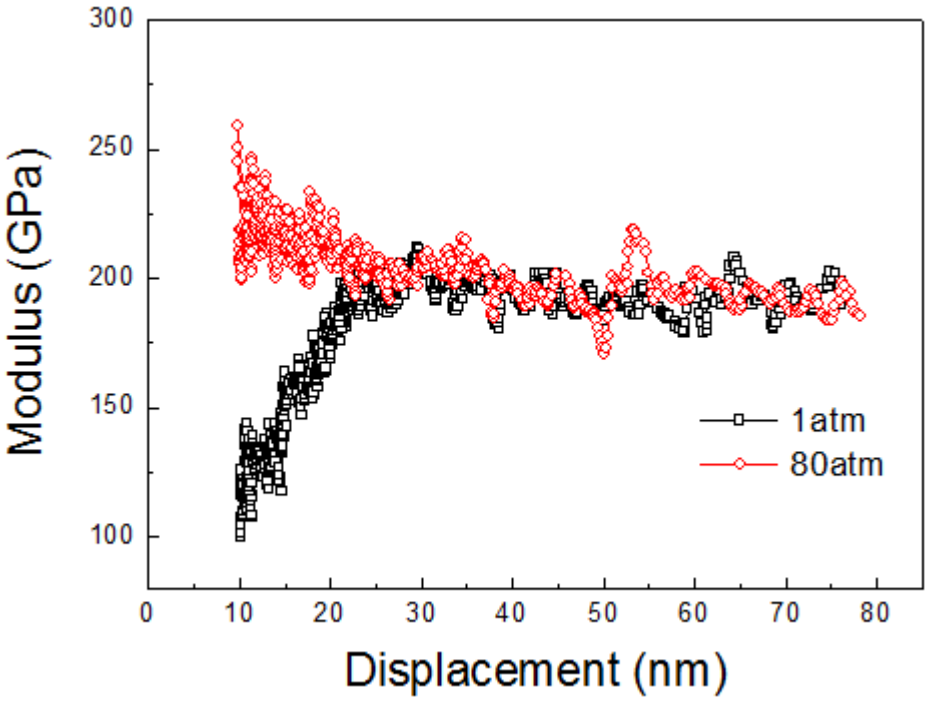

Figure 8. Elastic modulus of passive film of 316L SS formed at various hydrostatic pressures

The hardness and elastic modulus of passive film of 316L SS formed at various hydrostatic pressures were illustrated in Fig.7 and Fig.8, respectively. The passive film formed at 80 atm hydrostatic pressure showed higher value level of hardness and elastic modulus, implying superior mechanical properties, which indicated that the passive film formed at 80 atm hydrostatic pressure was more difficult to fracture that that at 1 atm pressure. This suggested that the passive film formed at 80 atm hydrostatic pressure had a higher corrosion resistance [36, 37].

3.3. Effect of hydrostatic pressure on pitting initiation of 316L SS

The time when current increase rapidly is the induction time (τ). Repetition of the same experiment yielded a number of induction time values.

The pitting formation event has been widely known to be a stochastic process. T. Shibata presented a stochastic theory of pitting corrosion based upon sensitivity analysis of parameters in the stochastic model that could rationally explain stochastic distributions of induction time for pitting formation [23-29]. In the stochastic model, the pitting formation process does not fit a simple exponential distribution, but could be explained by assuming series or parallel combinations of the simple birth stochastic process and birth/death process. The proposed models can be divided into two groups [23-29]: (1) Pure birth stochastic models, which only consider pitting generation events; (2) Birth and death stochastic models, which assume stochastic pitting generation and pitting repassivation.

Table 2. Analytical expressions of the survival probability function for various stochastic models.

Model	Survival probability function
Birth process A1 simple A2 series A3 parallel A4 combination	 $P(t)=\exp[-\lambda(t-t_0)]$ $P(t)=\exp[-m\lambda(t-t_0)]$ $P(t) =1-\{1-\exp[-\lambda(t-t_0)]\}^{m}$ $P(t) = \Sigma f_i \exp[-\lambda_i(t-t_0)]$
Birth and death process B1 parallel B2 series	 $P(t) =\mu/(\lambda+\mu) +\lambda/(\lambda+\mu) \exp[-(\lambda+\mu)(t-t_0)]$ $P(t) = \exp[-\alpha\lambda(t-\tau_c) \exp(-\mu\tau_c)]$

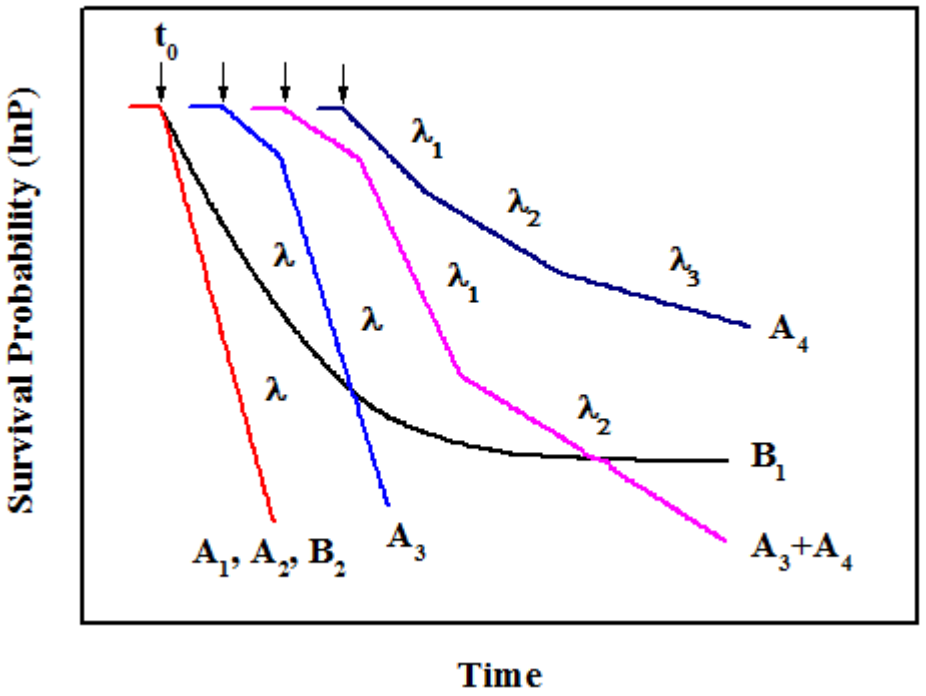

Figure 9. A schematic illustration of ln P_{sur} vs time of various stochastic models.

The expected equations for the survival probability, $P_{sur,}$ and time for pitting formation formulated for each model are shown in Table 2 [23-29] and corresponding curves between ln(P_{sur}) and time for each mode are illustrated in Fig. 9 [23-29].

Fig. 10 showed the logarithm of the survival probability, P_{sur}, as a function of induction time, *t*, for 316L SS at 1 atm and 80 atm pressure, respectively. This distribution type was the specific character of the combination of B1 model (parallel birth and death stochastic model) and A3 model (parallel birth stochastic model). In the other word, the plots of the distribution of induction time for 316L SS at various hydrostatic pressures exhibited analogue shape, which suggested that hydrostatic pressure did not change the pitting initiation mechanism.

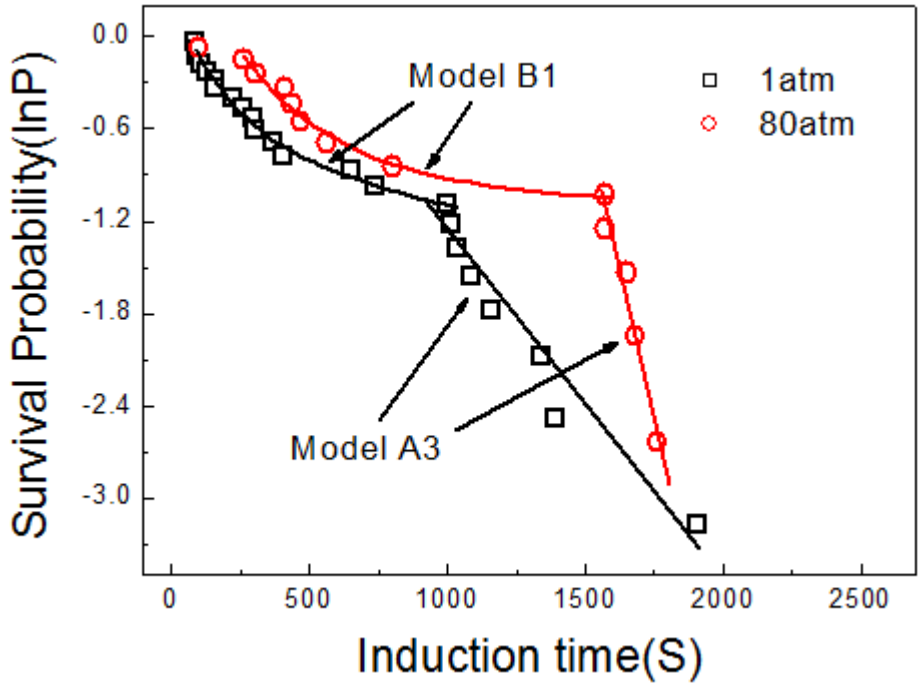

Figure 10. Plots of survival probability, P_{sur}, vs time for 316L SS at various hydrostatic pressures.

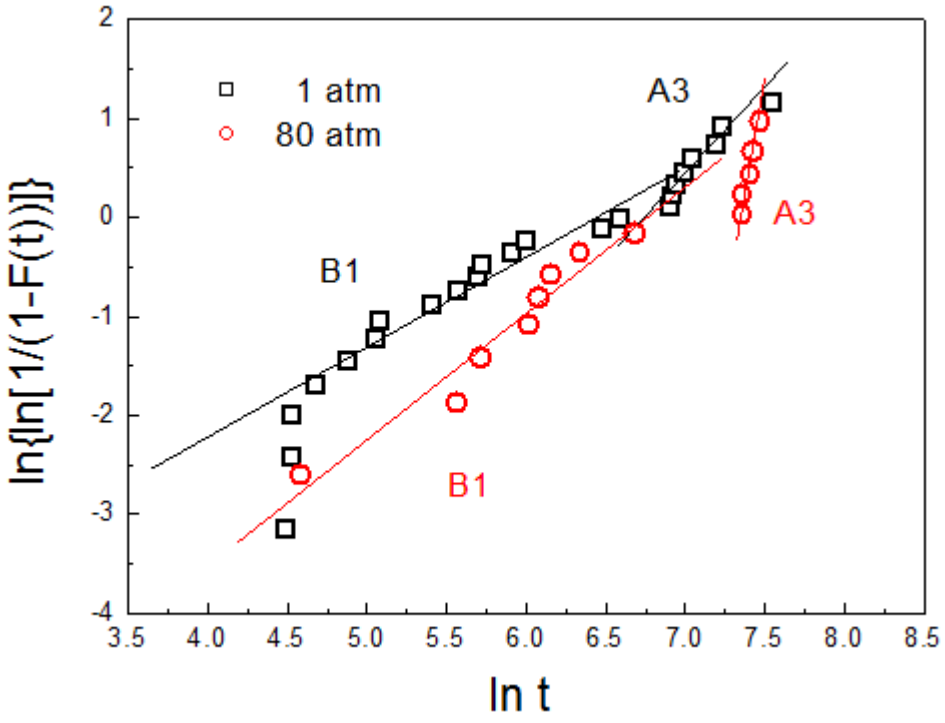

Figure 11. Weibull distribution for pitting induced time of 316L SS at various hydrostatic pressures.

Pitting corrosion initiation is modeled using a nonhomogeneous Poisson process [38, 39]. In this way, the distribution of corrosion induction times can be simulated using the Weibull distributions. Weibull distribution function is one of the widely used cumulative probability functions for predicting

life time in reliability test 40]. This is because it can easily approximate the normal distribution, logarithmic normal distribution and exponential distribution functions. In addition, it is also possible to analyze data even when two or more failure modes are present at the same time. The cumulative probability *F(t)* of a failure system can be introduced just as Weibull distribution function based upon a "weakest-link" model [40-42], which is expressed as

$$F(t) = 1 - \exp\left(-t^m / n\right) \quad (2)$$

where *m* and *n* are the shape and scale parameters, respectively. From rearrangement of Eq. (2):

$$\ln\{\ln[1/(1-F(t))]\} = m\ln t - \ln n \quad (3)$$

By fitting Eq. (3) to the cumulative probability numerically calculated, two parameters m and n can be determined from the slope of the linear ln {ln [1/(1-*F(t)*)]} versus ln *t* plots and from the intercept on the ln {ln [1/(1- *F(t)*)]} axis, respectively.

The Weibull probability plots for 316L SS at various hydrostatic pressures were shown in Fig. 11. Both plots showed satisfactorily good two straight lines. These two slopes represent two limiting cases corresponding to corrosion initiation process dominant B1 model and A3 model, respectively. From Fig. 11, the values of *m* and *n* for corrosion initiation dominant by different stochastic model were quantitatively determined, which were listed in Table 3.

Table 3. Weibull distribution parameters of pure magnesium in the absence and presence of magnetic field.

Hydrostatic pressure	Stochastic model	Shape parameters *m*	Location parameters *n*
1 atm	B1	0.855	248.668
	A3	2.013	97841.099
80 atm	B1	0.849	335.640
	A3	1.127	2612.806

According to stochastic theory, it may be possible to predict the generation probability of events in the future from the past events. This is so-called "the conditional probability". Based upon a stochastic theory, the corrosion initiation rate could be calculated by [43-45]:

$$r(t) = \frac{m}{n} t^{m-1} \quad (4)$$

The value of *r(t)*(/s) represents the rate of the corrosion initiation process dominant by different stochastic model in the next unit time for the specimens. The rate *r(t)* was determined by inserting the values of the shape and scale parameter m and n given in Table 3, into Eq. (4).

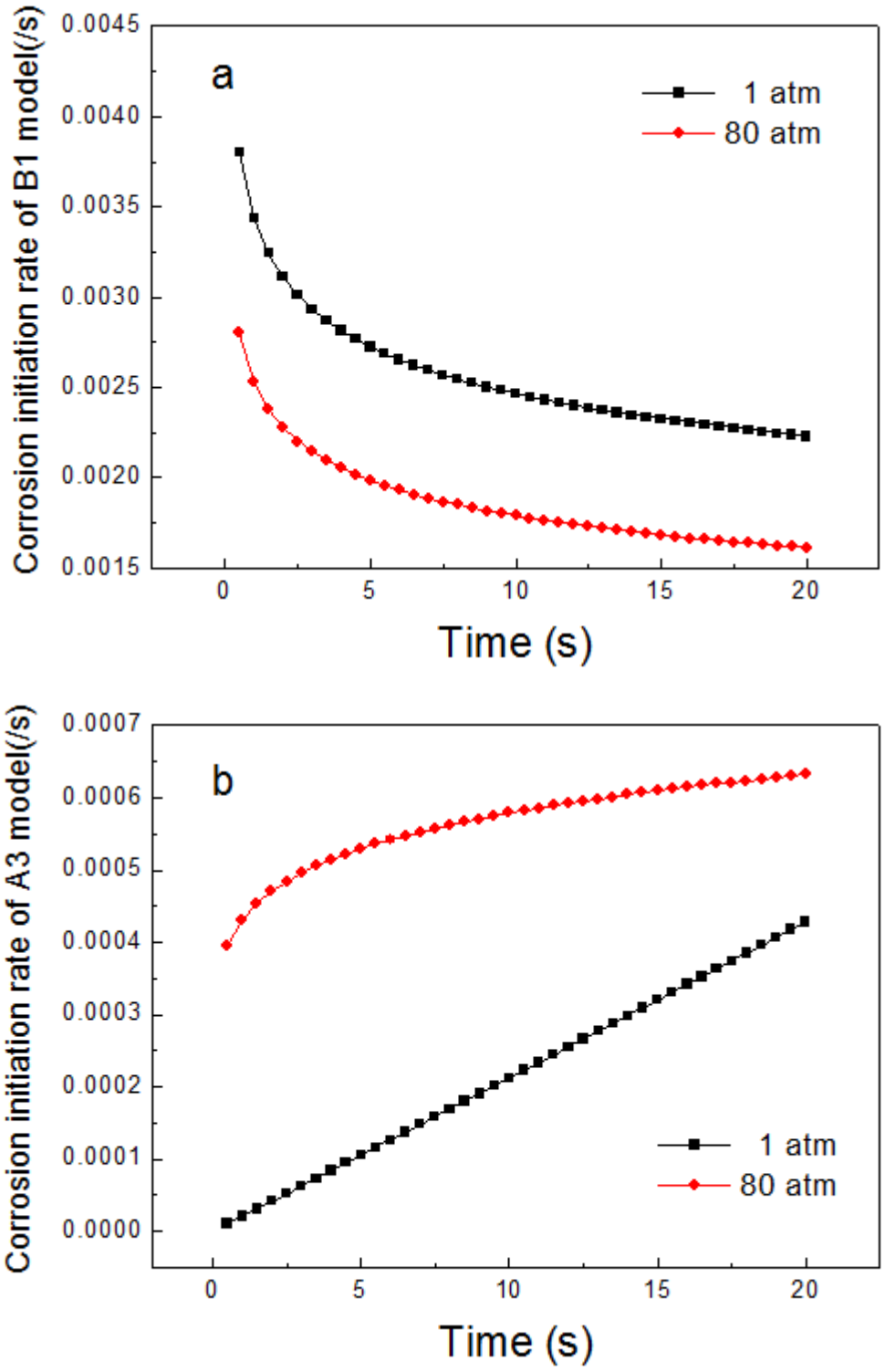

Figure 12. Plots of the pitting initiation rate for 316L SS at various hydrostatic pressures.

The resulting rate for corrosion initiation, *r(t)*, was illustrated in Fig. 12. It was observed that the corrosion initiation rate of A3 model was increased with hydrostatic pressure, while, the corrosion initiation rate of B1 model decreased with hydrostatic pressure.

3.4. Effect of hydrostatic pressure on pitting geometry of 316L SS

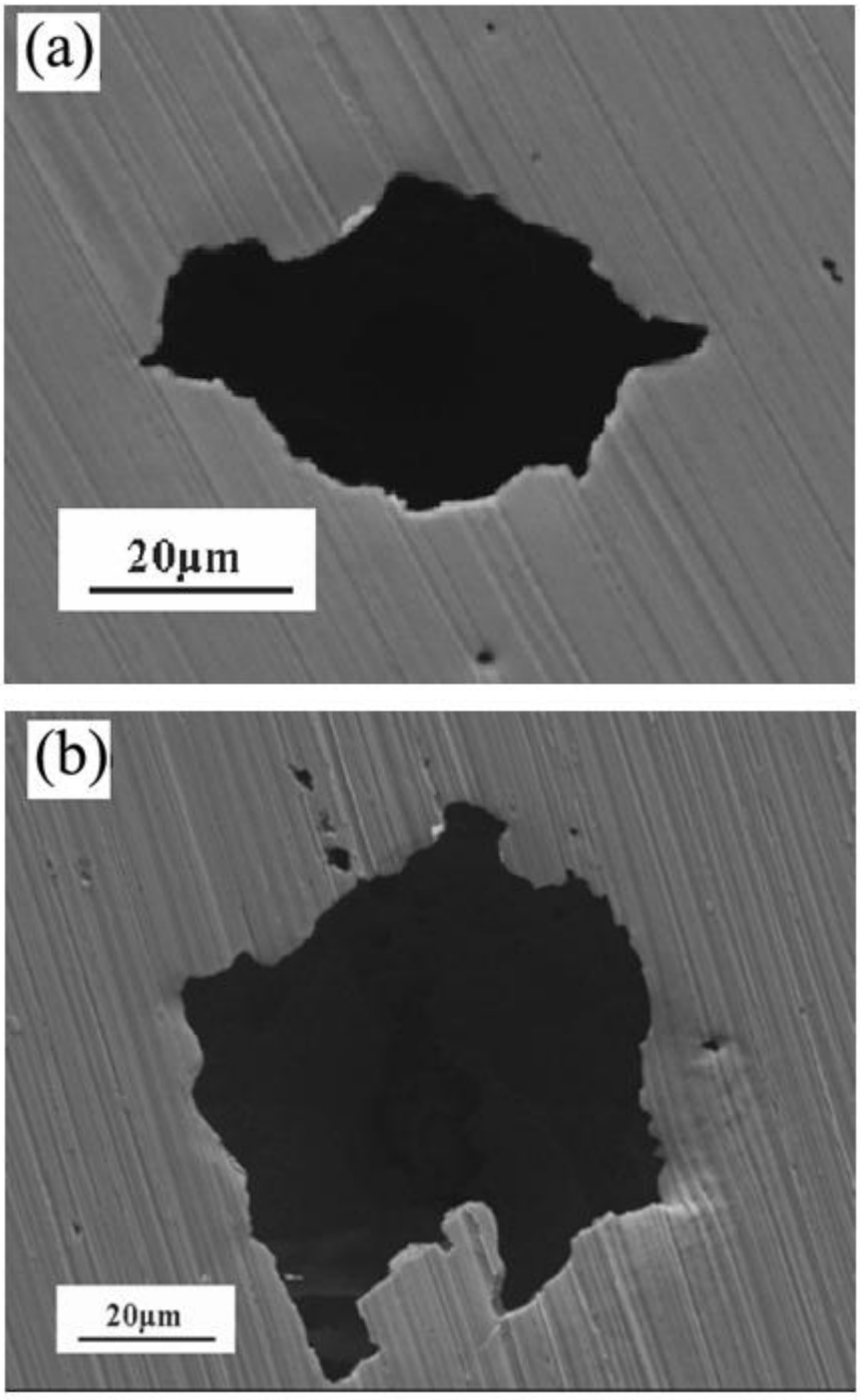

Figure 13. pitting corrosion morphology of 316L SS at various hydrostatic pressures.

The pitting corrosion morphology of 316L SS was illustrated in Fig.13. The pitting mouth size and pitting depth were measured by applying the Fine Focus Technique [35].

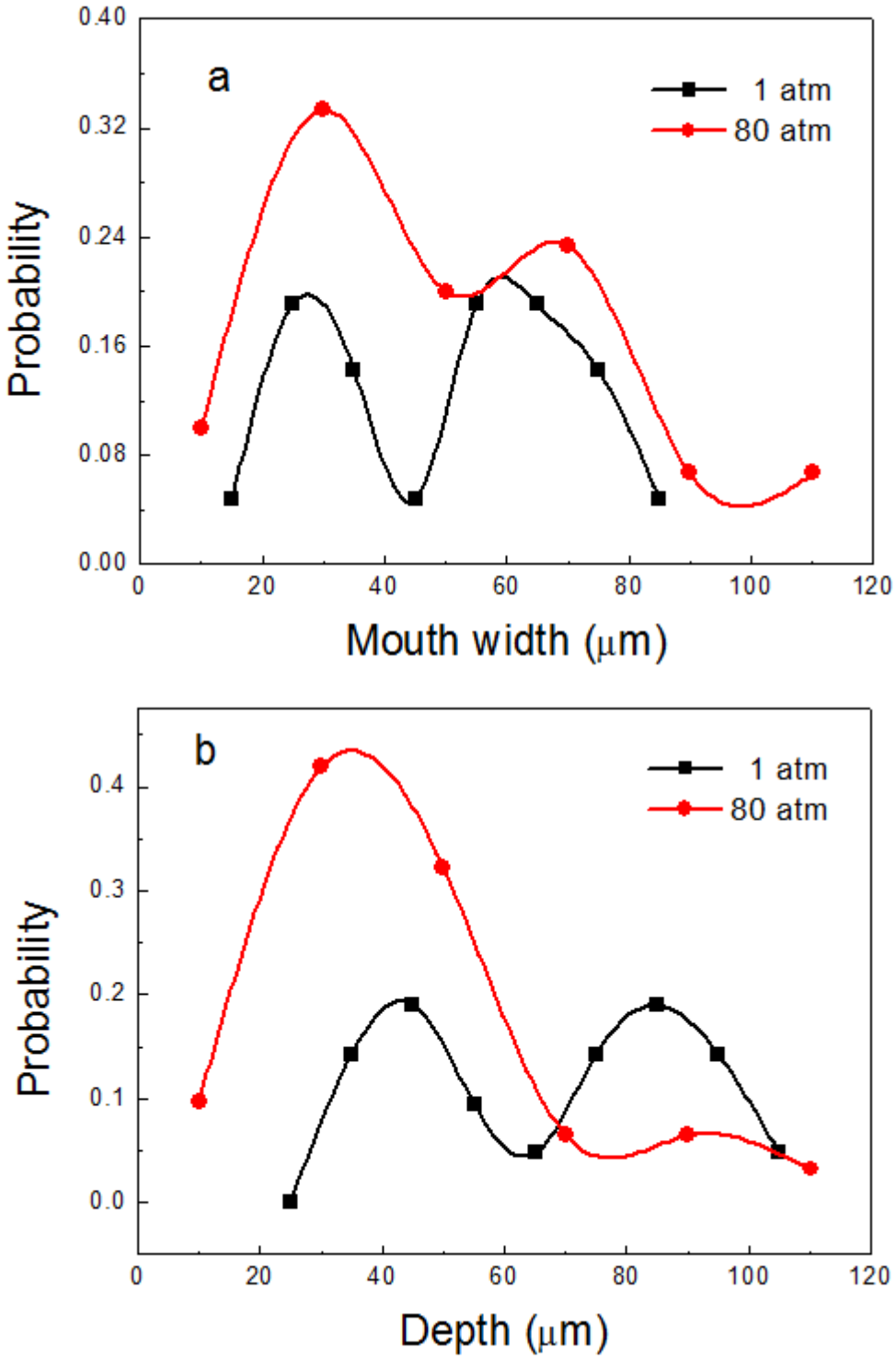

Figure 14. The distributions of (a) pitting mouth size and (b) pitting depth of 316L SS at various hydrostatic pressures.

The distributions of the pitting mouth size and pitting depth of 316L SS at various hydrostatic pressures were graphically represented in Fig.14. Fig.14 indicated that the pitting mouth size was increased with the increasing of hydrostatic pressure; meanwhile, the pitting depth was decreased with hydrostatic pressure.

Some scientists suggested that the pitting geometry could be described by the ratio of pitting mouth size *s* and pitting depth *h* (*s*/2*h*) [46-48]:

s/2*h* <1, pitting geometry exhibits deep-hole shape;

s/2*h* =1, pitting geometry shows hemispherical shape;

s/2*h* >1, pitting geometry demonstrates shallow-disk shape;

The schematic illustration of pitting geometry was exhibited in Fig.15.

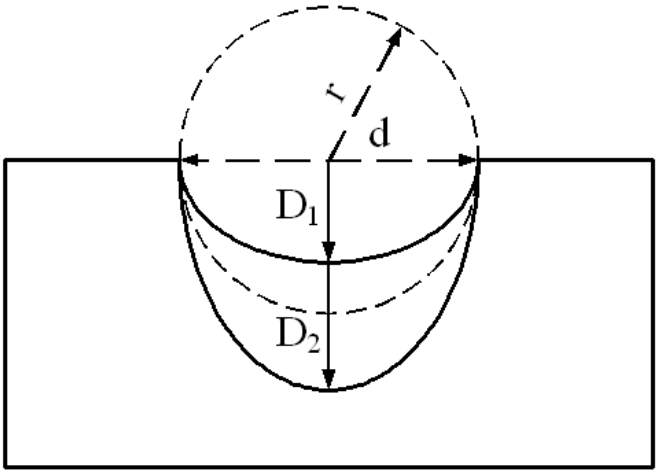

Figure 15. A schematic illustration of pitting geometry, *s*/2*h* <1, pitting geometry exhibits deep-hole shape; *s*/2*h* =1, pitting geometry shows hemispherical shape; *s*/2*h* >1, pitting geometry demonstrates shallow-disk shape.

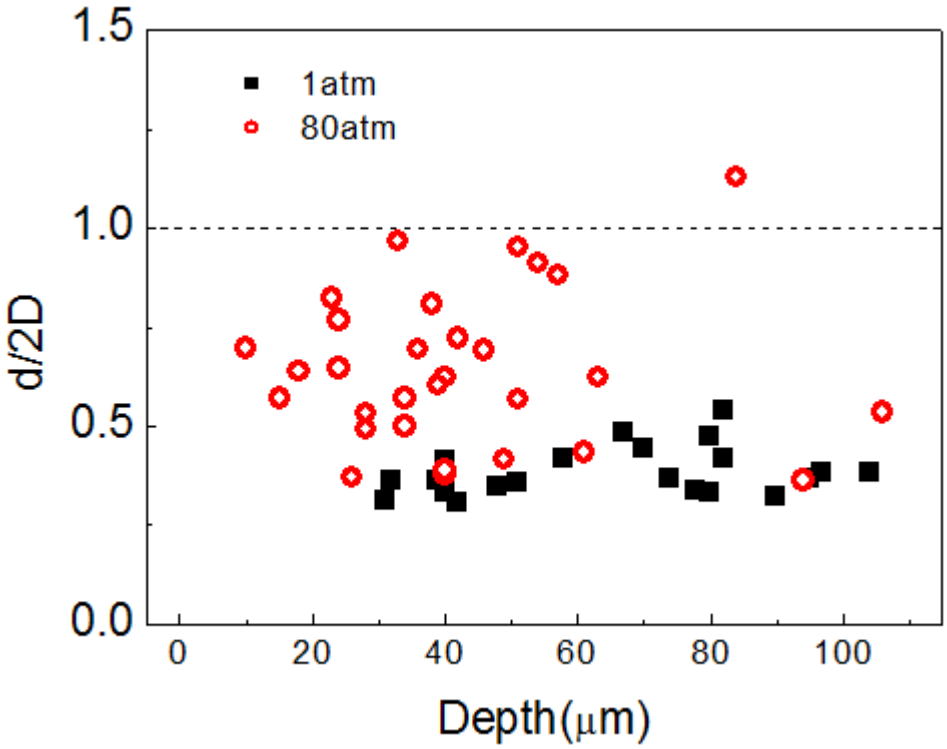

Figure 16. The pitting geometry of 316L SS at different hydrostatic pressure.

Fig.16 showed the pitting geometry of 316L SS at different hydrostatic pressures. The ratio of measured pitting mouth width to depth *s*/2*h* did depend upon the hydrostatic pressure and increased significantly with increasing hydrostatic pressure. At 1 atm hydrostatic pressure, *s*/2*h* data distributed around 0.35, implying the geometry of pitting cavity characterized as deep-hole shape. However, with the increasing hydrostatic pressure, the pitting geometry of 316L SS was distinguished by hemispherical shape and deep-hole shape (s/2*h* data ranged form 0.36 to 1.13).

The results of Fig.16 indicated that the hydrostatic pressure had significant influence on the type of pitting geometry. The increasing hydrostatic pressure increased the probability of hemispherical shape pitting cavity.

3.5. Effect of hydrostatic pressure on pitting growth of 316L SS

After the induction time, a sudden current rise was observed, which suggested that a stable pit had formed and grown. Pit growth is usually modeled using a nonhomogeneous Markov process [38]. To do this, the theoretical foundations of extreme value statistics have been employed. It is shown that the solution of the Kolmogorov forward equations, governing the growth of an individual pit, is in the domain of attraction of the Gumbel distribution [38].

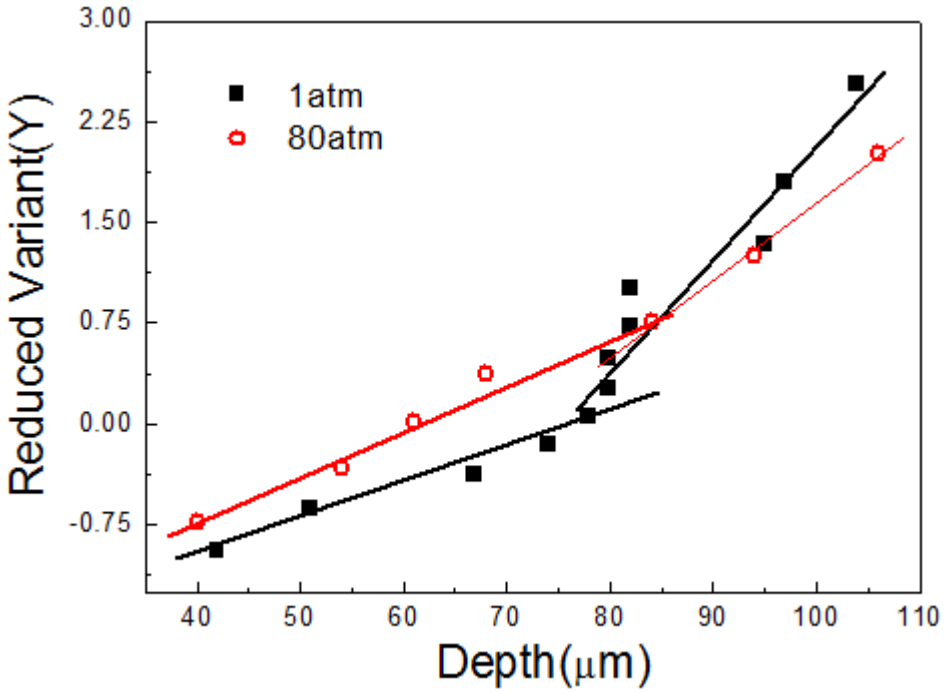

Figure 17. Gumbel probability plots of 316L SS at different hydrostatic pressure.

In many applications, the Gumbel Type distribution has been claimed to account for the stochastic nature in the observed behavior of corrosion systems [38, 39, 49-51].

The extreme value statistics analysis can be estimated according to the following procedure [51,52]: first, all calculated extreme value data are arranged in order from the smallest, and then the

probability F(Y) is calculated as 1-[M/(N + 1)], where M is the rank in the ordered extreme value and N the total number of extreme value data. The reduced variant (Y) can be calculated by the formula Y=-ln {-ln [F(Y)]}.

The probability that the largest value of pit depth is described by a double exponent (Gumbel Type extreme value distribution) can be calculated by the following form equations [51,52].

$$Pit_{\max} = \mu + \alpha \ln S \quad (5)$$

$$\text{Probability of pitting depth} = 1 - \exp\{ -\exp [\frac{\text{-(pitting depth-}[\mu + \alpha \ln S])}{\alpha}]\} \quad (6)$$

where μ is the central parameter (the most frequent value), S is the specimen area and α is the scale parameter, which defines the width of the distribution.

The largest pit depth within each of the potentiostatic measurements were determined by Fine Focus Technique [35] and the values were subjected to extreme value statistics analysis. The values of the reduced variant were plotted against the ordered pitting depth in Fig.17. Fig.17 distinctly showed two linear regions in one plot, which indicated that two kinds of pitting growth mechanism (deep-hole shape and hemispherical shape) undertook on 316L SS surface. The observation of straight line confirmed that the experimental data did in fact fit the Gumbel distribution. The values of α and μ are the scale and location parameters for the distribution of the largest pitting cavities respectively. These values are analogous to the standard deviation and average, and describe the shape and centre of the probability distribution of the maximum stable pitting depth expected from electrodes identical to those used for the measurements and are treated in the same manner for the same period of time. The scale and location parameters measured under various hydrostatic pressures were shown in Table 4.

Table 4. Gumbel distribution parameters for pure magnesium in the absence and presence of magnetic field.

Hydrostatic pressure	Maximum pitting depth （μm）	Location parameters α （μm）	Scale parameters λ （μm）
1atm	X<78	40.388	79.128
	X≥78	12.323	74.686
80atm	X<86	28.421	60.943
	X≥86	17.420	71.371

The probability of a given pitting depth occurring under various hydrostatic pressures was calculated using Eq. (6) and the results were shown in Fig. 18. The probabilities could be converted into an expected time for a pitting cavity with a particular depth to occur by taking the reciprocal of the probability. That is, calculating the time it takes for the cumulation of the probabilities to equal unity. For example, a 50 μm pitting depth under 1 atm hydrostatic pressure will occur on average after 46 min, but under 80 atm hydrostatic pressure, the average time for the same 50 μm pitting depth to occur is 55 min. A 75 μm pitting depth under 1 atm hydrostatic pressure will occur on average after 46 min, but under under 80 atm hydrostatic pressure the average time for the same 75 μm pitting depth to occur

is 122 min. These results indicate that a pitting formed on 316L SS had a lower probability of developing into a larger pitting cavity at higher hydrostatic pressure than at lower hydrostatic pressure.

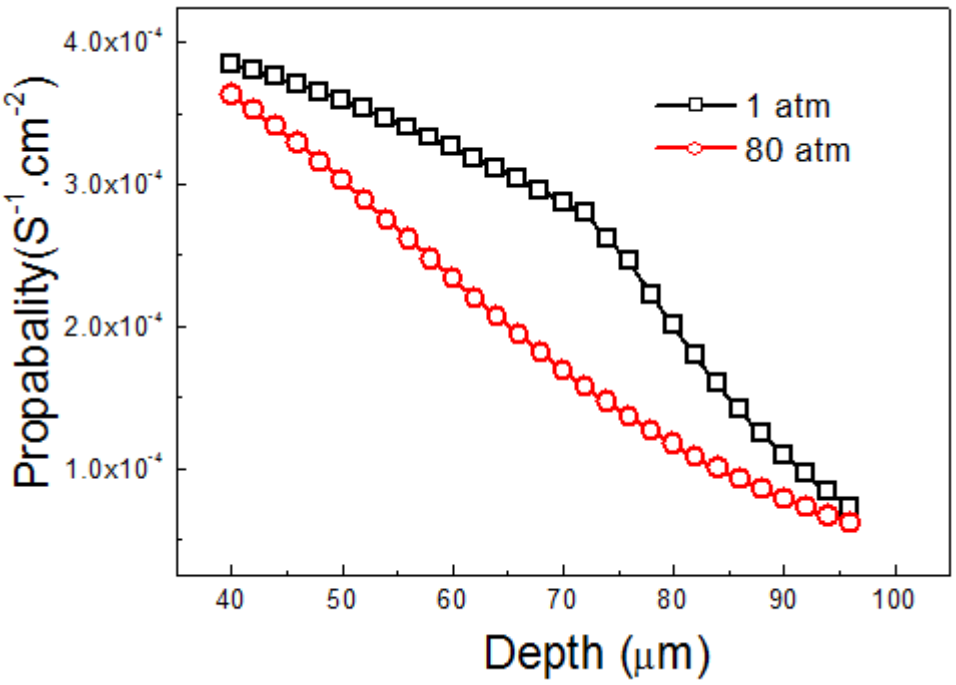

Figure 18. Probabilities of various depth pittings occurring on 316L SS at various hydrostatic pressures.

4. CONCLUSION

Both potentiodynamic polarization and EIS results indicated that the corrosion resistance of 316L SS was improved with the increasing hydrostatic pressure.

In case of higher hydrostatic pressure, both the hardness and elastic modulus of the passive film on 316L SS were increased, which indicated that the passive formed at higher hydrostatic pressure was difficult to fracture than that formed at lower hydrostatic pressure.

The pitting initiation mechanism was the combination of B1 model (parallel birth and death stochastic model) and A3 model (parallel birth stochastic model). B1 and A3 model related to deep-hole shape and hemispherical shape pitting cavity, respectively. The pitting initiation rate was analyzed based on Weibull distribution function. The increasing hydrostatic pressure retarded the B1 process, meanwhile, accelerated the pitting initiation process of A3 model.

The pitting growth process was analyzed based on extreme value statistics using Gumbel distribution function. The increasing hydrostatic pressure decreased the pitting growth probability. In case of higher hydrostatic pressure, pitting on 316L SS surface was more difficult to develop into a deeper cavity.

ACKNOWLEDGEMENTS
The authors wish to acknowledge the financial support of the Hundred Talents Program of Chinese Academy of Sciences and the National Natural Science Foundation of China (No. 51371182).

References

1. I. Ulanovskii, *Prot. Met*. 15 (1979) 563.
2. I. Ulanovskii, V. Egorova, *Prot. Met*. 14 (1978) 137.
3. F. Reinhart, J. Jenkins, "Corrosion of materials in surface seawater after 12 and 18 months," Technical Note N-1213, Naval Civil Engineering Laboratory, Port Hueneme, CA, 1972.
4. M. Schumacher: Sea Water Corrosion Handbook, Noyes Data, New Jersey, 1979, 107.
5. S. Chen, W. Hartt, S. Wolfson, *Corros.* 59 (2003) 721.
6. S. Dexter, *Corros.* 36 (1980) 423.
7. R. Venkatesan, M. Venkatasamy, T. Bhaskaran, E. Dwarakadasa, *Br. Corros. J.* 37 (2002) 257.
8. S. Sawant, A. Wagh, *Corros. Prevent. Contr.* 37 (1990) 154.
9. A.M. Beccaria, G. Poggi, G. Castello, *Br. Corros. J.* 21 (1986) 19.
10. A.M. Beccaria, P. Fiordiponti, D. Mattongno, *Corros. Sci*. 29 (1989) 403.
11. A.M. Beccaria, G. Poggi, D. Gingaud, P. Castello, *Br. Corros. J.* 29 (1994) 65.
12. A.M. Beccaria, G. Poggi, M. Arfelli, D. Mattongno, *Corros. Sci.* 34 (1993) 989.
13. A.M. Beccaria, G. Poggi, G. Castello, *Br. Corros. J.* 30 (1995) 283.
14. S. Chen, W. Hartt, *Corros*. 58 (2002) 38.
15. A.M. Beccaria, G. Poggi, *Br. Corros. J.* 20 (1985) 183.
16. T. Zhang, Y. Yang, Y. Shao, G. Meng, F. Wang, *Electrochim.Acta*.54 (2009) 3915.
17. B. Liu, T. Zhang, Y. Shao, G. Meng, F. Wang, *Mater. Corros.* 62 (2011) 269.
18. B. Liu, T. Zhang, Y. Shao, G. Meng, F. Wang, *Int. J. Electrochem. Sci.*, 7 (2012) 1864.
19. Y. Yang, T. Zhang, Y. Shao, G. Meng, F. Wang, *Corros. Sci.* 52 (2010) 2697.
20. Y. Yang, T. Zhang, Y. Shao, G. Meng, F. Wang, *Corros. Sci.* 73 (2013) 250.
21. S. Hu, T. Zhang, Y. Shao, G. Meng, F. Wang, *Anti-Corros. Method. Mater.* 58 (2011) 238.
22. T. Shibata, T. Takeyama, *Nature*, 260 (1976) 315.
23. T. Shibata, *Corros*., 52 (1996)813
24. T. Shibata, Y. Zhu, *Corros. Sci.* 36 (1994) 153
25. T. Shibata, M. Ameer, *Corros. Sci*. 33 (1992) 1633.
26. T. Shibata, *Corros. Sci***.** 31 (1990) 413.
27. T. Shibata, Y. Zhu, *Corros. Sci.* 36 (1994) 1735.
28. T. Shibata, Y. Zhu, *Corros. Sci.* 37 (1995) 853.
29. S. Fujimoto, T. Shibata, M. Minamida, S. Udaka, *Corros. Sci.* 36 (1994) 1575.
30. F. Wall, M. Martinez, *J. Electrochem. Soc*., 150(2003) B146.
31. T. Zhang, C. Chen, Y. Shao, G. Meng, F. Wang, *Electrochim. Acta*, 53 (2008)7921.
32. T. Zhang, X. Liu, Y. Shao, G. Meng, F. Wang, *Corros. Sci.* 50 (2008) 3500.
33. G. Meng, L. Zhang, Y. Shao, T. Zhang, F. Wang, *Corros. Sci.* 51 (2009) 1685.
34. G. Meng, L. Wei, Y. Shao, T. Zhang, F. Wang, *J. Electrochem. Soc*., 156(2009) C240.
35. ASTM Stand G46-94(2005), "Standard Guide for Examination and Evaluation of Pitting Corrosion," ASTM International,West Conshohocken, PA.
36. A. Alamr, D. Bahr，M. Jacroux, *Corros. Tech. Sci. Eng*., 40(2005)255
37. A. Alamr, D. Bahr，M. Jacroux, *Corros. Sci*. 48 (2006) 925
38. A. Valor, F. Caleyo, L. Alfonso, D. Rivas, J. Hallen, *Corros. Sci.* 49 (2007) 559
39. G. Engelhardt, D. Macdonald, *Corros. Sci*. 46 (2004) 2755
40. E. Lewis, Introduction to Reliability Engineering, John Wiley and Sons, New York, 1987.
41. S. Pyun, E. Lee, G. Han, *Thin Solid Films* 239 (1994) 74

42. J. Park, S. Pyun, *Corros. Sci*. 46 (2004) 285-296
43. K. Na, S. Pyun, *Electrochim. Acta* 52 (2007) 4363-4373
44. K. Na, S. Pyun, *Corros. Sci*. 49 (2007) 2663-2675
45. K. Na, S. Pyun, *Corros. Sci*. 50 (2008) 248-258
46. D. Sun, Y. Jiang, Y. Tang, Q. Xiang, C. Zhong, J. Liao, J. Li, *Electrochim. Acta*, 54 (2009) 1558
47. M. Moayed, R. Newman, *J. Electrochem. Soc.,* 153 **(**2006) B330
48. P. Pistorius, G. Burstein, *Phil. Trans. R. Soc. Lond*. A**,** 341 (1992) 531
49. A. Turnbull, *Br. Corros. J*. 28 (1993) 297.
50. A. Tahara, T. Shinohara, *Corros. Sci*. 47 (2005) 2589
51. A. Trueman, *Corros. Sci*. 47 (2005) 2240
52. Z. Wang, Y. Cong, T. Zhang, Y. Shao, G. Meng, *Int. J. Electrochem. Sci.*, 6 (2011) 5521.